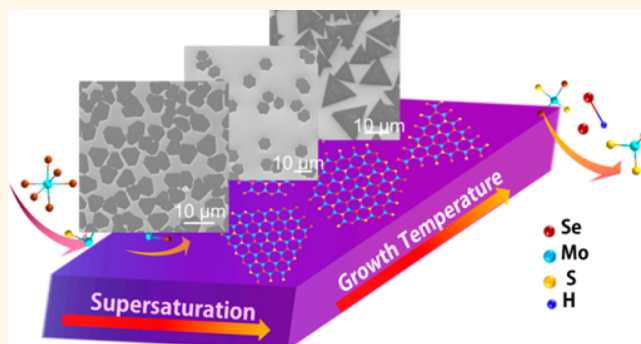


# Growth of $\text{MoS}_{2(1-x)}\text{Se}_{2x}$ ( $x = 0.41 - 1.00$ ) Monolayer Alloys with Controlled Morphology by Physical Vapor Deposition

Qingliang Feng,<sup>†,‡,§</sup> Nannan Mao,<sup>†</sup> Juanxia Wu,<sup>†</sup> Hua Xu,<sup>||</sup> Chunming Wang,<sup>§</sup> Jin Zhang,<sup>\*,†</sup> and Liming Xie<sup>\*,‡</sup>

<sup>†</sup>Center for Nanochemistry, Beijing Science and Engineering Center for Nanocarbons, Beijing National Laboratory for Molecular Sciences, College of Chemistry and Molecular Engineering, Peking University, Beijing 100871, P. R. China, <sup>‡</sup>CAS Key Laboratory of Standardization and Measurement for Nanotechnology, National Center for Nanoscience and Technology, Beijing 100190, P. R. China, <sup>§</sup>School of Chemistry and Chemical Engineering, Lanzhou University, Lanzhou 730000, P. R. China, and <sup>||</sup>School of Materials Science and Engineering, Shaanxi Normal University, Xi'an 710119, P. R. China

**ABSTRACT** Transition-metal dichalcogenide (TMD) monolayer alloys are a branch of two-dimensional (2D) materials which can have large-range band gap tuning as the composition changes. Synthesis of 2D TMD monolayer alloys with controlled composition as well as controlled domain size and edge structure is of great challenge. In the present work, we report growth of  $\text{MoS}_{2(1-x)}\text{Se}_{2x}$  monolayer alloys ( $x = 0.41 - 1.00$ ) with controlled morphology and large domain size using physical vapor deposition (PVD).  $\text{MoS}_{2(1-x)}\text{Se}_{2x}$  monolayer alloys with different edge orientations (Mo-zigzag and S/Se-zigzag edge orientations) have been obtained by controlling the deposition temperature. Large domain size of  $\text{MoS}_{2(1-x)}\text{Se}_{2x}$  monolayer alloys ( $x = 0.41 - 1.00$ ) up to  $20 \mu\text{m}$  have been obtained by tuning the temperature gradient in the deposition zone. Together with previously obtained  $\text{MoS}_{2(1-x)}\text{Se}_{2x}$  monolayer alloys ( $x = 0 - 0.40$ ), the band gap photoluminescence (PL) is continuously tuned from 1.86 eV (i.e., 665 nm, reached at  $x = 0.00$ ) to 1.55 eV (i.e., 800 nm, reached at  $x = 1.00$ ). Additionally, Raman peak splitting was observed in  $\text{MoS}_{2(1-x)}\text{Se}_{2x}$  monolayer alloys. This work provides a way to synthesize  $\text{MoS}_{2(1-x)}\text{Se}_{2x}$  monolayer alloys with different edge orientations, which could be benefit to controlled growth of other 2D materials.



**KEYWORDS:** physical vapor deposition ·  $\text{MoS}_{2(1-x)}\text{Se}_{2x}$  · alloy · morphology · tunable band gap · Raman spectrum

Two-dimensional (2D) transition-metal dichalcogenides (TMDs) have potential applications in water splitting, optoelectronics and nanoelectronics for their special edge effect, superior optical and electrical properties.<sup>1–6</sup> Both theoretical calculation and experimental work have shown that the band gap of 2D TMDs alloys can be tuned in a wide spectrum range by changing the composition.<sup>7,8</sup> Several approaches have been developed to synthesize 2D alloys, such as mechanical exfoliation of the bulk alloy crystals,<sup>9,10</sup> chemical vapor deposition (CVD),<sup>11–13</sup> and physical vapor deposition (PVD).<sup>14</sup> CVD and PVD can produce large single crystal domains and continuous films of 2D alloys, which are more preferred for spectroscopic and

electrical investigations.<sup>15–17</sup> The primary challenge in the synthesis is to precisely control the composition as well as the domain size and the edge orientation.<sup>1,4,18–22</sup> In CVD growth of  $\text{MoS}_2$  monolayers *via* sulfurization of  $\text{MoO}_3$ , sulfur pressure can affect the morphology of  $\text{MoS}_2$  monolayers,<sup>23,24</sup> in which  $\text{MoS}_2$  monolayers with the straight edges and the inward curving edges, corresponding to Mo-zigzag and S-zigzag edge orientations, respectively, have been obtained.<sup>25</sup>

Previously, we reported direct PVD growth of  $\text{MoS}_{2(1-x)}\text{Se}_{2x}$  monolayer alloys but with limited Se content ( $x = 0 - 0.40$ ).<sup>14</sup> The difficulty for synthesizing  $\text{MoS}_{2(1-x)}\text{Se}_{2x}$  monolayer alloys with high Se content arises from decomposition of  $\text{MoSe}_2$  to

\* Address correspondence to  
xielm@nanoctr.cn,  
jinzhang@pku.edu.cn.

Received for review April 26, 2015  
and accepted June 10, 2015.

Published online June 10, 2015  
10.1021/acsnano.5b02506

© 2015 American Chemical Society

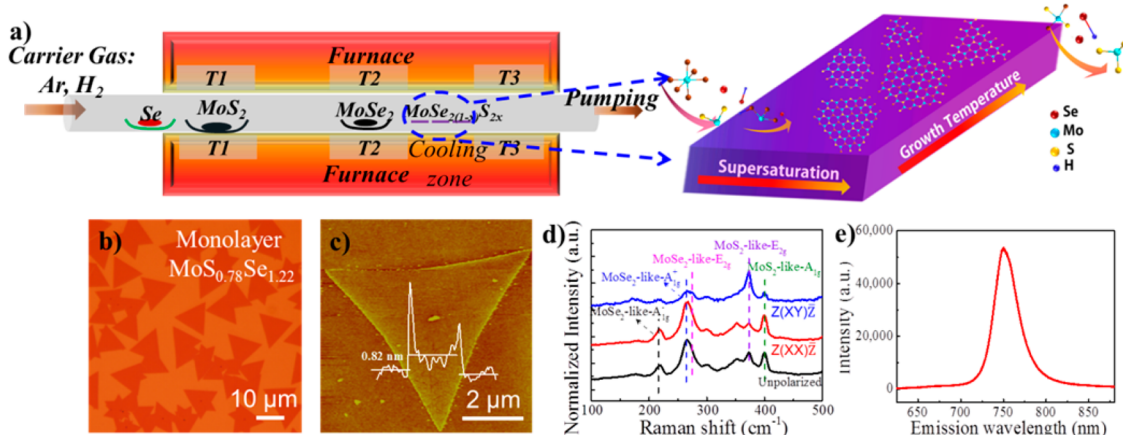


**Figure 1.** (a) Illustration of three-zone furnace setup for  $\text{MoS}_{2(1-x)}\text{Se}_{2x}$  ( $x = 0.41 - 1.00$ ) monolayer growth. (b) Optical image, (c) AFM image, (d) polarized Raman spectra, and (e) PL spectrum of as-grown  $\text{MoS}_{0.78}\text{Se}_{1.22}$  monolayers.

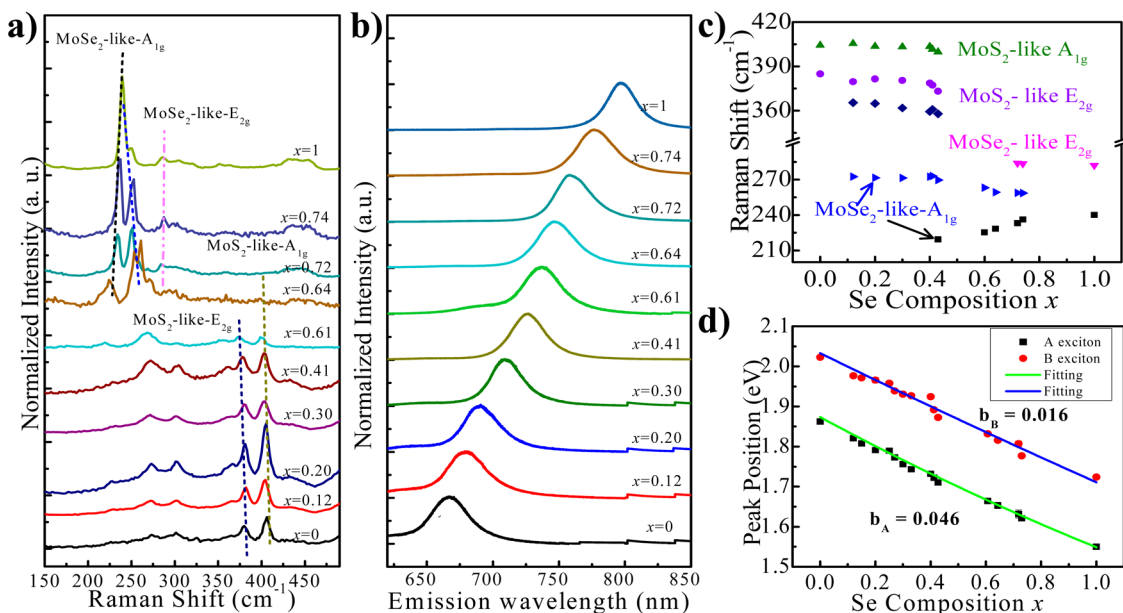


**Figure 2.** Spectroscopic characterizations of  $\text{MoS}_{2(1-x)}\text{Se}_{2x}$  monolayers. (a) Raman spectra, (b) PL spectra of  $\text{MoS}_{2(1-x)}\text{Se}_{2x}$  monolayers ( $x = 0.00 - 1.00$ ). (c) Plots of Raman frequency shift against the Se composition  $x$  in  $\text{MoS}_{2(1-x)}\text{Se}_{2x}$  monolayers. (d) Plots of A-, B-exciton emission energy of  $\text{MoS}_{2(1-x)}\text{Se}_{2x}$  monolayers against the Se composition  $x$ . The data of Se composition  $x$  ( $x = 0.00 - 0.40$ ) is similar to our previous reported data.<sup>14</sup>

$\text{Mo}_3\text{Se}_4$  at high temperatures. So a Se-rich condition is necessary to inhibit the decomposition.<sup>26,27</sup> Here, by adding Se vapor during PVD, we have obtained  $\text{MoS}_{2(1-x)}\text{Se}_{2x}$  monolayer alloys with Se content  $x$  of 0.41–1.00. Further, the  $\text{MoS}_{2(1-x)}\text{Se}_{2x}$  monolayers with large domain sizes and different edge orientations (Mo-zigzag and S/Se-zigzag edge orientations) have been obtained by tuning the deposition parameters (such as the temperature gradient in the deposition zone and the deposition temperature).

## RESULTS AND DISCUSSION

Figure 1a illustrates the growth process. Se powders were put in the upstream of the furnace with temperature about 300 °C.  $\text{MoS}_2$  and  $\text{MoSe}_2$  powders were put in the first and second zones, respectively, and directly

vaporized at high temperatures (950–965 °C).  $\text{SiO}_2/\text{Si}$  substrates (oxide thickness of ~270 nm) were put in the deposition zone with lower temperatures ( $T \sim 600 - 770$  °C). By fine controlling growth conditions, such as evaporation temperature, temperature gradient in the deposition zone, and the deposition temperature (Supporting Information Figure S1), we grew large-size high-crystalline  $\text{MoS}_{2(1-x)}\text{Se}_{2x}$  ( $x = 0.41 - 1.00$ ) monolayers directly on  $\text{SiO}_2/\text{Si}$  substrates. Figure 1b shows a typical optical image of as-grown  $\text{MoS}_{0.78}\text{Se}_{1.22}$  monolayers.

The Se composition in  $\text{MoS}_{2(1-x)}\text{Se}_{2x}$  monolayers was determined by X-ray photoelectron spectroscopy (XPS, Supporting Information Figure S2). Atomic force microscopic (AFM) imaging showed a height of around 0.8 nm for as-grown  $\text{MoS}_{0.78}\text{Se}_{1.22}$  monolayers

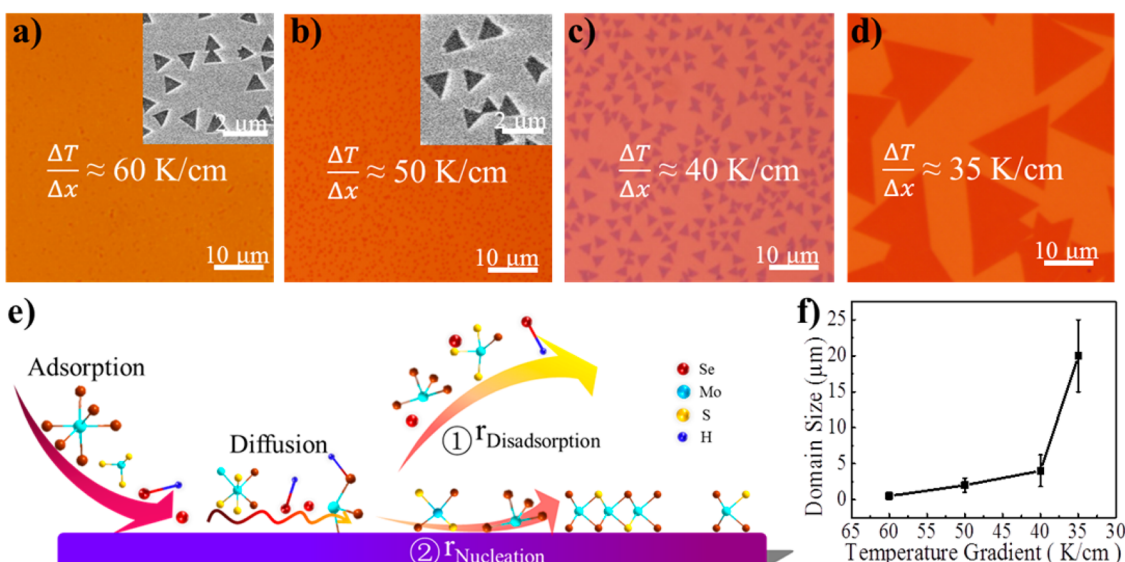


**Figure 3.** Tuning domain size of  $\text{MoS}_{2(1-x)}\text{Se}_{2x}$  monolayers by changing the temperature gradient in the deposition zone. Morphologies of  $\text{MoS}_{0.78}\text{Se}_{1.22}$  triangles obtained at temperature gradient of (a) 60, (b) 50, (c) 40, and (d) 35  $^{\circ}\text{C}/\text{cm}$ . (e) Schematic illustration of the growth process. (f) The domain size of as-synthesized  $\text{MoS}_{0.78}\text{Se}_{1.22}$  monolayer domains against the temperature gradient in the deposition zone.

(Figure 1c). Five intense Raman peaks were observed from  $\text{MoS}_{0.78}\text{Se}_{1.22}$  monolayers (Figure 1d). The  $402 \text{ cm}^{-1}$  peak (active only at  $Z(\bar{X}\bar{X})\bar{Z}$ ) is assigned to  $\text{MoS}_2$ -like  $A_{1g}$  mode. The  $373 \text{ cm}^{-1}$  (active at both  $Z(\bar{X}\bar{X})\bar{Z}$  and  $Z(\bar{X}\bar{Y})\bar{Z}$ ) is assigned to  $\text{MoS}_2$ -like  $E_{2g}$  mode. The peaks at  $219$  and  $267 \text{ cm}^{-1}$  (active only at  $Z(\bar{X}\bar{X})\bar{Z}$  configuration) are assigned to  $\text{MoSe}_2$ -like  $A_{1g}$  modes. The Raman peaks at  $276 \text{ cm}^{-1}$  (active at both  $Z(\bar{X}\bar{X})\bar{Z}$  and  $Z(\bar{X}\bar{Y})\bar{Z}$ ) is assigned to  $\text{MoSe}_2$ -like  $E_{2g}$ .  $\text{MoS}_{0.78}\text{Se}_{1.22}$  monolayer showed strong PL emission at about  $750 \text{ nm}$  (*i.e.*,  $1.65 \text{ eV}$ , Figure 1e), indicating the direct band gap nature.

Raman and PL mapping were conducted to investigate the composition homogeneity of  $\text{MoS}_{0.78}\text{Se}_{1.22}$  monolayer domains (Supporting Information Figure S3). PL emission at  $750 \text{ nm}$  and Raman peak at  $268 \text{ cm}^{-1}$  shows homogeneous intensity within the same individual domains. For different domains, PL peak wavelength and Raman peak frequency show a variation of  $\pm 2 \text{ nm}$  and  $\pm 1 \text{ cm}^{-1}$ , respectively, indicating homogeneous composition within a large area.

Figure 2a shows composition dependent Raman spectra of  $\text{MoS}_{2(1-x)}\text{Se}_{2x}$  monolayers. The  $\text{MoSe}_2$ -related Raman branches and  $\text{MoS}_2$ -related Raman branches are well separated. There is splitting of  $\text{MoSe}_2$ -like  $A_{1g}$  and  $\text{MoS}_2$ -like  $E_{2g}$ , which is similar to that in  $\text{MoS}_{2(1-x)}\text{Se}_{2x}$  bulk crystals.<sup>28</sup> The splitting arises from different coordination configurations of Se/S around Mo. Figure 2c shows composition-dependent Raman frequencies. In detail, the low-frequency  $\text{MoSe}_2$   $A_{1g}$  mode continuously shifts from  $241$  to  $219 \text{ cm}^{-1}$  as the Se composition  $x$  changes from  $1.00$  to  $0.40$ . The high-frequency  $\text{MoSe}_2$ -like  $A_{1g}$  continuously shifts from  $241$  to  $275 \text{ cm}^{-1}$  as the Se composition  $x$  changes from  $1$  to  $0.1$ . The  $\text{MoSe}_2$ -like  $E_{2g}$  shifts from  $287.1$  to

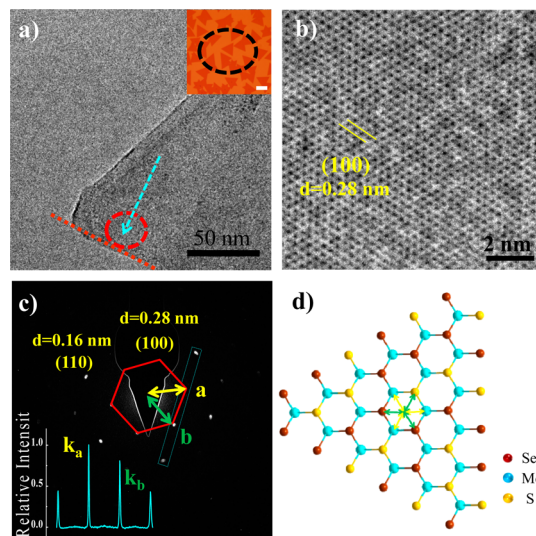


**Figure 4.** TEM imaging of  $\text{MoS}_{0.78}\text{Se}_{1.22}$  monolayers. (a) TEM image and (b) HRTEM image of  $\text{MoS}_{0.78}\text{Se}_{1.22}$  monolayers. The inset in panel (a) is an optical image of  $\text{MoS}_{0.78}\text{Se}_{1.22}$  monolayers. (c) SAED pattern for the  $\text{MoS}_{0.78}\text{Se}_{1.22}$  monolayer in panel (a), in which the higher intensity  $k_a$  spots correspond to the Mo sublattice, and  $k_b$  spots correspond to the S/Se sublattice. (d) Schematic illustration of atomic structure for the  $\text{MoS}_{0.78}\text{Se}_{1.22}$  domain in panel (a).

$281.9 \text{ cm}^{-1}$  as the Se composition changes from  $1$  to  $0.64$ . The  $\text{MoS}_2$ -like  $A_{1g}$  mode shifts from  $403.0$  to  $399 \text{ cm}^{-1}$  as the Se composition  $x$  changes from  $0.0$  to  $0.43$ . The  $\text{MoS}_2$   $E_{2g}$  mode continuously shifts from  $384.1$  to  $373.5 \text{ cm}^{-1}$  as the Se composition  $x$  changes from  $0.0$  to  $0.43$ .

Figure 2b shows PL spectra of as-grown  $\text{MoS}_{2(1-x)}\text{Se}_{2x}$  ( $x = 0$ – $1.00$ ) monolayers. The emission energy can be continually tuned from  $1.86 \text{ eV}$  ( $665 \text{ nm}$ ) to  $1.55 \text{ eV}$  ( $800 \text{ nm}$ ). Plots of A-, B-exciton emission energy against

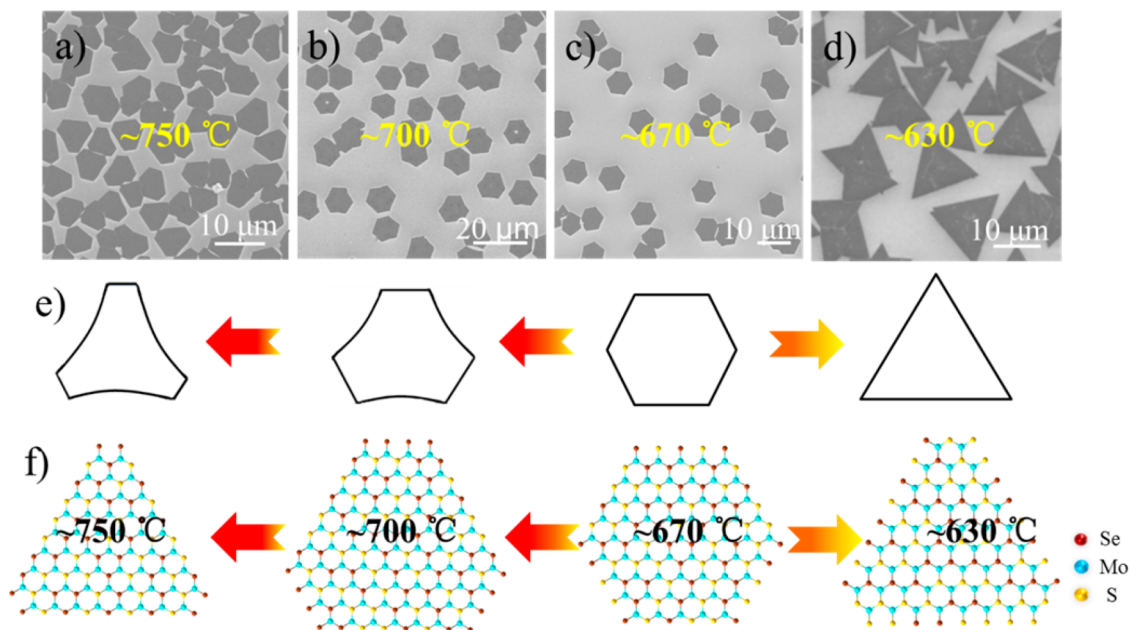


**Figure 5.** SEM images of  $\text{MoS}_{0.78}\text{Se}_{1.22}$  domains obtained at different deposition temperatures: (a)  $\sim 750$ , (b)  $\sim 700$ , (c)  $\sim 670$ , and (d)  $\sim 630$  °C (temperature gradient fixed at 35 °C/cm). (e) Schematic illustration of different morphologies at deposition temperatures. (f) Proposed structures for domains obtained at different deposition temperatures.

the Se composition  $x$  were shown in Figure 2d. As the Se composition  $x$  increases, PL emission wavelength shows a redshift. The band gap bowing effect in  $\text{MoS}_{2(1-x)}\text{Se}_{2x}$  monolayer alloys is not significant (bowing parameter  $\sim 0.046$  eV, Figure 2d).

The growth process of 2D monolayers on substrates involves nucleation and growth. In the nucleation process, supersaturation is the most important parameter. In the growth process, several steps are involved, including adsorption/desorption of monomers, diffusion and reaction (Figure 3e). In our PVD experiments, supersaturation can be controlled by temperature gradient in the deposition zone. Figure 3a–d shows optical images of as-prepared  $\text{MoS}_{0.78}\text{Se}_{1.22}$  monolayers at different deposition gradients. At high temperature gradients, supersaturation is larger and more nucleation is expected, which results in smaller  $\text{MoS}_{0.78}\text{Se}_{1.22}$  monolayer domains. At low temperature gradients, supersaturation is small and less nucleation is expected, which results in large  $\text{MoS}_{0.78}\text{Se}_{1.22}$  monolayer domains. For example, at lowest temperature gradient of our system ( $\sim 35$  °C/cm),  $\text{MoS}_{0.78}\text{Se}_{1.22}$  monolayers with size of more than 10  $\mu\text{m}$  were obtained.

TEM and selected area electron diffraction (SAED) were conducted to characterize the edge orientation of as-grown monolayers. Figure 4a,b shows TEM images of a  $\text{MoS}_{0.78}\text{Se}_{1.22}$  triangle. The HRTEM image (Figure 4b) shows (100) lines with spacing of 0.28 nm and (110) lines with spacing of 0.16 nm. The SAED pattern (Figure 4c) shows only one set of hexagon spots, indicating single-crystal nature of the  $\text{MoS}_{0.78}\text{Se}_{1.22}$  domain. The inset image in Figure 4c

was a line profile through experimentally measured diffraction spots. According to reference work,<sup>25</sup>  $k_a$  spots with higher intensity correspond to the Mo sublattice (indicated by the arrows in a), and  $k_b$  spots with lower intensity correspond to the dichalcogenide (Se, S) sublattice (indicated by the arrows in b). This infers that the edge orientation of the triangle should be along Mo-zigzag direction (Figure 4d). Similar experimental data for  $\text{MoSe}_2$  monolayers is shown in Supporting Information Figure S4.

At different deposition temperatures (temperature gradient fixed at 35 °C/cm), different morphologies of  $\text{MoS}_{0.78}\text{Se}_{1.22}$  monolayers were observed (Figure 5a). Triangles with straight edge were obtained at low temperatures such as 630 °C (Figure 5d). At intermediate temperatures such as 670 °C, hexagons with straight edges were obtained (Figure 5c). At high temperatures such as 750 °C, triangles with inward curving edges were obtained (Figure 5a). Similar experimental results were also observed in the growth of  $\text{MoSe}_2$  and  $\text{MoS}_2$  monolayers (Supporting Information Figure S4), suggesting that the morphology is only dependent on the deposition temperature but not on the composition. TEM and SAED characterizations revealed that the straight edges of  $\text{MoS}_{0.78}\text{Se}_{1.22}$  triangles obtained at 630 °C are along Mo-zigzag edge orientation. The inward curving edges obtained at 750 °C is along S/Se-zigzag edge orientation. The preferred edge orientation observed at different deposition temperatures (*i.e.*, at different deposition positions) may relate to different chemical potentials of Se ( $\mu_{\text{Se}}$ ) along the deposition zone.<sup>23,29,30</sup>

## CONCLUSION

We have successfully grown  $\text{MoS}_{2(1-x)}\text{Se}_{2x}$  ( $0.41 \leq x \leq 1.00$ ) monolayer alloys with controlled size and edge orientation *via* tuning PVD parameters. Larger  $\text{MoS}_{2(1-x)}\text{Se}_{2x}$  monolayer domains ( $10\text{--}20 \mu\text{m}$ ) can be obtained at lower temperature gradients in the deposition zone. At a fixed temperature gradient, lower deposition temperatures can give domains with the

Mo-zigzag edges, while higher temperatures can give domains with the S/Se-zigzag edges. Moreover, composition-dependent Raman behavior in  $\text{MoS}_{2(1-x)}\text{Se}_{2x}$  alloys has also been investigated. Raman splitting was observed in  $\text{MoS}_{2(1-x)}\text{Se}_{2x}$  monolayer alloys. This work gives insight for PVD growth of 2D TMD alloys with controlled composition, large domain size and specific edge orientation.

## METHODS

**Sample Growth.**  $\text{MoS}_{2(1-x)}\text{Se}_{2x}$  ( $x = 0.41\text{--}1.00$ ) monolayers were synthesized by evaporation of  $\text{MoSe}_2$  powders (Sigma-Aldrich, 99.95%,  $40 \mu\text{m}$ ) put in the first zone and  $\text{MoS}_2$  powders (Sigma-Aldrich, 99%,  $< 2 \mu\text{m}$ ) in the second heating zones. Se powders (Sigma-Aldrich, 99.999%,  $40 \mu\text{m}$ ) were put in the upstream of the furnace with the temperature about  $300^\circ\text{C}$ . The loading of Se,  $\text{MoS}_2$  and  $\text{MoSe}_2$  powders was usually  $10\text{--}100 \text{ mg}$ . The  $\text{SiO}_2/\text{Si}$  substrates (oxide thickness of  $\sim 270 \text{ nm}$ ) were put in the deposition zone which was between the second zone and the third zone. The deposition zone was at temperature of  $600\text{--}770^\circ\text{C}$ . The temperature gradient was tuned from  $\sim 60$  to  $\sim 35^\circ\text{C/cm}$  by setting the temperature of the third zone in the range of  $250\text{--}350^\circ\text{C}$ . The  $\text{SiO}_2/\text{Si}$  substrates were annealed at  $800^\circ\text{C}$  for 8 h. The carrier gases were Ar (2 sccm) and  $\text{H}_2$  (1 sccm). The pressure of the growth system was  $\sim 14 \text{ Pa}$ . The growth time was about 15 min.

**Characterization.** Optical images were taken on an Olympus BX51 microscope using a  $100\times$  objective. Tapping mode AFM was done on a DI 3100 multimode microscope. SEM imaging was done on a Hitachi S4800. Raman and PL spectra were measured on a JY Horiba HR800 micro-Raman spectrometer (514 nm excitation) under ambient conditions. XPS was done on an Axis Ultra system. The monolayers were transferred on to TEM microgrids. TEM images and SAED patterns were acquired on a Tecnai G2 F20 U-TWIN operated at 200 kV.

In the polarized Raman experiments, the parallel polarization, *i.e.*,  $Z(\bar{X}\bar{X})\bar{Z}$  configuration, was measured by placing an analyzer between edge filter and detector, in which the polarization direction of the scattered light was parallel to that of the incident laser. The cross-polarization, *i.e.*,  $(Z\bar{X}Y)\bar{Z}$  configuration, was measured by placing a half-wave plate in the laser path and placing an analyzer between edge filter and detector in the signal path. The intensity and peak position of the PL and Raman peaks were fitted by Gaussian and Lorentzian functions, respectively.

**Conflict of Interest:** The authors declare no competing financial interest.

**Acknowledgment.** J.Z., L.X. and Q.F. designed the experiment. Q.F., N.M., J.W., H.X., and L.X. performed the experiments and analyzed the data. J.Z., L.X. and Q.F. contributed to the writing of the manuscript. L. Xie acknowledges support from NSFC (21373066 and 11304052), China Postdoctoral Science Foundation (2013M540900) and Beijing Nova Program (2015B049). J. Zhang acknowledges support from NSFC (21233001, 21129001, 51272006, and 51121091) and MOST (2011YQ0301240201 and 2011CB932601). C. Wang acknowledges the NSFC (No. 51372106) for financial support of this work.

**Supporting Information Available:** The PVD details, XPS spectra of  $\text{MoS}_{2(1-x)}\text{Se}_{2x}$  monolayer alloy, TEM images of as-synthesized  $\text{MoSe}_2$  monolayers, morphologies of  $\text{MoS}_2$  and  $\text{MoSe}_2$  monolayers, different morphologies of  $\text{MoS}_{0.78}\text{Se}_{1.22}$  monolayers. The Supporting Information is available free of charge on the ACS Publications website at DOI: 10.1021/acsnano.5b02506.

## REFERENCES AND NOTES

- Yin, X.; Ye, Z.; Chenet, D. A.; Ye, Y.; O'Brien, K.; Hone, J. C.; Zhang, X. Edge Nonlinear Optics on a  $\text{MoS}_2$  Atomic Monolayer. *Science* **2014**, *344*, 488–490.
- Fuhrer, M. S.; Hone, J. Measurement of Mobility in Dual-Gated  $\text{MoS}_2$  Transistors. *Nat. Nanotechnol.* **2013**, *8*, 146–147.
- Radisavljevic, B.; Whitwick, M. B.; Kis, A. Integrated Circuits and Logic Operations Based on Single-Layer  $\text{MoS}_2$ . *ACS Nano* **2011**, *5*, 9934–9938.
- Kibsgaard, J.; Chen, Z.; Reinecke, B. N.; Jaramillo, T. F. Engineering the Surface Structure of  $\text{MoS}_2$  to Preferentially Expose Active Edge Sites for Electrocatalysis. *Nat. Mater.* **2012**, *11*, 963–969.
- Mak, K. F.; He, K.; Shan, J.; Heinz, T. F. Control of Valley Polarization in Monolayer  $\text{MoS}_2$  by Optical Helicity. *Nat. Nanotechnol.* **2012**, *7*, 494–498.
- Radisavljevic, B.; Radenovic, A.; Brivio, J.; Giacometti, V.; Kis, A. Single-Layer  $\text{MoS}_2$  Transistors. *Nat. Nanotechnol.* **2011**, *6*, 147–150.
- Kang, J.; Tongay, S.; Li, J.; Wu, J. Monolayer Semiconducting Transition Metal Dichalcogenide Alloys: Stability and Band Bowing. *J. Appl. Phys.* **2013**, *113*, 143703.
- Komsa, H.-P.; Krasheninnikov, A. V. Two-Dimensional Transition Metal Dichalcogenide Alloys: Stability and Electronic Properties. *J. Phys. Chem. Lett.* **2012**, *3*, 3652–3656.
- Chen, Y.; Xi, J.; Dumcenco, D. O.; Liu, Z.; Suenaga, K.; Wang, D.; Shuai, Z.; Huang, Y. S.; Xie, L. Tunable Band Gap Photoluminescence from Atomically Thin Transition-Metal Dichalcogenide Alloys. *ACS Nano* **2013**, *7*, 4610–4616.
- Zhang, M.; Wu, J.; Zhu, Y.; Dumcenco, D. O.; Hong, J.; Mao, N.; Deng, S.; Chen, Y.; Yang, Y.; Jin, C.; et al. Two-Dimensional Molybdenum Tungsten Diselenide Alloys: Photoluminescence, Raman Scattering, and Electrical Transport. *ACS Nano* **2014**, *8*, 7130–7137.
- Mann, J.; Ma, Q.; Odenthal, P. M.; Isarraraz, M.; Le, D.; Preciado, E.; Barroso, D.; Yamaguchi, K.; Von Son Palacio, G.; Nguyen, A.; et al. 2-Dimensional Transition Metal Dichalcogenides with Tunable Direct Band Gaps:  $\text{MoS}_{2-x}\text{Se}_{2x}$  Monolayers. *Adv. Mater.* **2014**, *26*, 1399–1404.
- Li, H.; Duan, X.; Wu, X.; Zhuang, X.; Zhou, H.; Zhang, Q.; Zhu, X.; Hu, W.; Ren, P.; Guo, P.; et al. Growth of Alloy  $\text{MoS}_{2-x}\text{Se}_{2(1-x)}$  Nanosheets with Fully Tunable Chemical Compositions and Optical Properties. *J. Am. Chem. Soc.* **2014**, *136*, 3756–3759.
- Gong, Y.; Liu, Z.; Lupini, A. R.; Shi, G.; Lin, J.; Najmaei, S.; Lin, Z.; Elías, A. L.; Berkdemir, A.; You, G.; et al. Band Gap Engineering and Layer-by-Layer Mapping of Selenium-Doped Molybdenum Disulfide. *Nano Lett.* **2014**, *14*, 442–449.
- Feng, Q.; Zhu, Y.; Hong, J.; Zhang, M.; Duan, W.; Mao, N.; Wu, J.; Xu, H.; Dong, F.; Lin, F.; et al. Growth of Large-Area 2D  $\text{MoS}_{2(1-x)}\text{Se}_{2x}$  Semiconductor Alloys. *Adv. Mater.* **2014**, *26*, 2648–2653.
- Yu, Y.; Li, C.; Liu, Y.; Su, L.; Zhang, Y.; Cao, L. Controlled Scalable Synthesis of Uniform, High-Quality Monolayer and Few-Layer  $\text{MoS}_2$  Films. *Sci. Rep.* **2013**, *3*, No. 1866.
- Zhang, J.; Yu, H.; Chen, W.; Tian, X.; Liu, D.; Cheng, M.; Xie, G.; Yang, W.; Yang, R.; Bai, X.; et al. Scalable Growth of

- High-Quality Polycrystalline MoS<sub>2</sub> Monolayers on SiO<sub>2</sub> with Tunable Grain Sizes. *ACS Nano* **2014**, *8*, 6024–6030.
17. Wu, S.; Huang, C.; Aivazian, G.; Ross, J. S.; Cobden, D. H.; Xu, X. Vapor-Solid Growth of High Optical Quality MoS<sub>2</sub> Monolayers with Near-Unity Valley Polarization. *ACS Nano* **2013**, *7*, 2768–2772.
18. Li, Y.; Zhou, Z.; Zhang, S.; Chen, Z. MoS<sub>2</sub> Nanoribbons: High Stability and Unusual Electronic and Magnetic Properties. *J. Am. Chem. Soc.* **2008**, *130*, 16739–16744.
19. Splendiani, A.; Sun, L.; Zhang, Y.; Li, T.; Kim, J.; Chim, C.-Y.; Galli, G.; Wang, F. Emerging Photoluminescence in Monolayer MoS<sub>2</sub>. *Nano Lett.* **2010**, *10*, 1271–1275.
20. Zhang, J.; Soon, J. M.; Loh, K. P.; Yin, J.; Ding, J.; Sullivan, M. B.; Wu, P. Magnetic Molybdenum Disulfide Nanosheet Films. *Nano Lett.* **2007**, *7*, 2370–2376.
21. Bollinger, M. V.; Lauritsen, J. V.; Jacobsen, K. W.; Nørskov, J. K.; Helveg, S.; Besenbacher, F. One-Dimensional Metallic Edge States in MoS<sub>2</sub>. *Phys. Rev. Lett.* **2001**, *87*, 196803.
22. Helveg, S.; Lauritsen, J. V.; Lægsgaard, E.; Stensgaard, I.; Nørskov, J. K.; Clausen, B. S.; Topsøe, H.; Besenbacher, F. Atomic-Scale Structure of Single-Layer MoS<sub>2</sub> Nanoclusters. *Phys. Rev. Lett.* **2000**, *84*, 951–954.
23. Wang, S.; Rong, Y.; Fan, Y.; Pacios, M.; Bhaskaran, H.; He, K.; Warner, J. H. Shape Evolution of Monolayer MoS<sub>2</sub> Crystals Grown by Chemical Vapor Deposition. *Chem. Mater.* **2014**, *26*, 6371–6379.
24. Najmaei, S.; Liu, Z.; Zhou, W.; Zou, X.; Shi, G.; Lei, S.; Yakobson, B. I.; Idrobo, J.-C.; Ajayan, P. M.; Lou, J. Vapour Phase Growth and Grain Boundary Structure of Molybdenum Disulphide Atomic Layers. *Nat. Mater.* **2013**, *12*, 754–759.
25. Van der Zande, A. M.; Huang, P. Y.; Chenet, D. A.; Berkelbach, T. C.; You, Y.; Lee, G.-H.; Heinz, T. F.; Reichman, D. R.; Muller, D. A.; Hone, J. C. Grains and Grain Boundaries in Highly Crystalline Monolayer Molybdenum Disulphide. *Nat. Mater.* **2013**, *12*, 554–561.
26. Chaouch, M.; Monnereau, O.; Vacquier, G.; Cerclier, R. O.; Casalot, A. Energy Photoconversion Using MoX<sub>2</sub> (X=S, Se) Electrodes. *Ann. Chim.* **1985**, *10*, 47–58.
27. Tarascon, J. M.; DiSalvo, F. J.; Murphy, D. W.; Hull, G.; Waszczak, J. V. New Superconducting Ternary Molybdenum Chalcogenides InMo<sub>6</sub>Se<sub>8</sub>, T1Mo<sub>6</sub>S<sub>8</sub>, and T1Mo<sub>6</sub>Se<sub>8</sub>. *Phys. Rev. B* **1984**, *29*, 172–180.
28. Jadczak, J.; Dumcenco, D. O.; Huang, Y. S.; Lin, Y. C.; Suenaga, K.; Wu, P. H.; Hsu, H. P.; Tiong, K. K. Composition Dependent Lattice Dynamics in MoS<sub>x</sub>Se<sub>(2-x)</sub> Alloys. *J. Appl. Phys.* **2014**, *116*, 193505.
29. Cao, D.; Shen, T.; Liang, P.; Chen, X.; Shu, H. Role of Chemical Potential in Flake Shape and Edge Properties of Monolayer MoS<sub>2</sub>. *J. Phys. Chem. C* **2015**, *119*, 4294–4301.
30. Füchtbauer, H.; Tuxen, A.; Li, Z.; Topsøe, H.; Lauritsen, J.; Besenbacher, F. Morphology and Atomic-Scale Structure of MoS<sub>2</sub> Nanoclusters Synthesized with Different Sulfiding Agents. *Top. Catal.* **2014**, *57*, 207–214.